Letters in Applied NanoBioScience
Open-Access Journal (ISSN: 2284-6808)

Article
Volume 13, Issue 4, 2024, 179
https://doi.org/10.33263/LIANBS134.179

A Battle Against Harmful Microbes - Study of Second Generation Dendrimer (G2) Stabilized Co@TiO_2 Core-Shell Nanoparticles with Effective Biological Activity

Shivani R. B [1], Pavithra. S [2], R. Vanathi Vijayalakshmi [2,*]

[1] Department of Physics, Presidency College, Chennai, India
[2] Department of Physics, Queen Mary's College, Chennai, India
[*] Correspondence: –vanathirgobinath@gmail.com, r.vanathivijayalakshmi@queenmaryscollege.edu.in;
Scopus Author ID 57202152002

Received: 19.08.2023; Accepted: 7.07.2024; Published: 28.08.2024

Abstract: Co@TiO_2 core-shell nanoparticles were synthesized using two different stabilizers, i.e., PVP (Co@TiO_2 – A) and second generation (G2) triazolyl chalcone dendrimer (Co@TiO_2 – B) by reduction transmetalation method. The structural parameters of the sample were analyzed using XRD, FTIR, and XPS techniques. The crystallite size and the lattice strain of the samples were calculated using the Scherrer formula, and the results were compared with the Size-Strain Plot (SSP). The optical studies show that the sample Co@TiO_2 – B has recorded a sharp absorption peak at 336 nm and exhibits a band gap of 3.06 eV, which is 0.28 eV wider than Co@TiO_2 – A. Photoluminescence study displays that when G_2 acts as a stabilizing agent the peak intensity increases without any peak shift. The biological study against the fungal pathogens reveals the significant role of Co@TiO_2 – B against *Candida albicans* for its strong antifungal activity.

Keywords: reduction transmetalation method; XRD; XPS; photoluminescence; *Candida albicans*.

1. Introduction

Dendrimers have become a study of interest among researchers of various fields due to their carrier-like nature, biocompatibility, and biodegradability [1]. They are also known as monodisperse, polyvalent, or usually globular macromolecules with a regular or highly-branched three-dimensional structure. These numerous positive attributes have made dendrimers a suitable carrier for the nano drug-delivery application, and thus, these dendrimers have taken the field of nanotechnology by storm. To emphasize this new trend, the annual publication rate for dendrimers is approximately 1000 publications [2,3]. In addition, dendrimers also help stabilize the capped nanoparticles from agglomerating. The structure of a dendrimer consists of three components: (a) the core or the nucleus, (b) generations (G) the originating layer called the dendrons, and (c) the surface, which is made of terminal groups [4]. This structure paves the way to load the drugs into them many numbers of times effectively [5]. Thus making it reusable and environmentally friendly [6,7].

Likewise, core-shell nanoparticles have attracted many researchers due to their high functionality, stability, dispersibility, and controlled release of the core [8]. These properties have major usage in pharmaceuticals and biomedical applications such as controlled drug delivery, specific targeting and bio-imaging, and electronic applications [9,10].

Several studies have revealed that among various transition metals [11], cobalt plays an important role in living and organic processes, which has resulted in human adaptation to cobalt overdose [12]. Biomedical studies proved that the cobalt nanoparticles lose their magnetic properties when entering the bloodstream and become a non-magnetic oxide [13]. This is possible because cobalt has probable oxidation states from -1 to +4. Each of these states displays varied properties, which can be engineered for different applications.

Similarly, TiO_2 has distinct properties as well. It has a stable ability to oxidize and reduce better permeability, and unique optical and electrical properties. Titanium dioxide (TiO_2) is mostly used in water treatment, where it has been observed to interact with contaminants such as cadmium, altering its level of toxicity and bio-availability [14]. With many metal oxide nanoparticles being studied for their biological applications, titanium dioxide has gained great interest due to its ability to attach itself to the affected cells, infiltrating them and finally causing the termination of the cell [15,16].

Candida albicans is often found inhibiting skin, gut, and urinary tract as a benign pathogen. When the condition of the host changes, especially when there is a lowering of immunity, Candida albicans becomes a harmful yet non-threatening pathogen, where immunity suppression is found to be its predominant symptom [17,18]. Aspergillus Niger is another opportunistic pathogen [19]. Various enzymes of Aspergillus niger have found their usage in biotechnological industries and play an effective role in various environmental factors such as limiting or inciting degradation of biomass and for the fermentation process [20].

However, Aspergillus niger has been found to aggravate morbid patient mortality, especially in those who are suffering from lung cancer. Thus, it is important to find new and effective medications to reduce the impact of the fungus, such as these opportunistic pathogens that lie inactive inside and outside of us [21]. In this paper, the combination of cobalt and titanium oxide is synthesized and characterized for phase, structural, and biological studies in combating these two opportunistic pathogens using dendrimers and achieving a core-shell structure [22–25].

2. Materials and Methods

2.1. Synthesis.

$Co@TiO_2$ core-shell nanoparticles were synthesized by reduction transmetalation method using two different stabilizers, i.e., PVP ($Co@TiO_2$ – A) and second generation (G2) triazolyl chalcone dendrimer ($Co@TiO_2$ – B). The reaction was carried out in a nitrogen atmosphere. Cobalt chloride ($CoCl_2.6H_2O$), Titanium (IV) oxide (TiO_2), Sodium borohydride ($NaBH_4$), and ethanol were purchased from Sigma-Aldrich Pvt. Ltd. The chemicals were used directly without further purification. Distilled water was used for the synthesis.

5 mg of second-generation (G2) triazolyl chalcone dendrimer is dissolved in 10 ml of chloroform and stirred for 20 min until the dendrimer is completely dissolved and the color of the solution turns deep yellow. 2g of $CoCl_2.6H_2O$ is dissolved in the above solution. 10 ml of reducing agent was prepared using 5 ml of 1M NaOH and 10 ml of 2M of $NaBH_4$. This was added drop by drop into the solution under a nitrogen atmosphere. After further stirring, 0.67g of TiO_2 was added, and the solution was stirred for 10-12 h. The sample was collected, repeatedly washed, centrifuged with organic solvents, and dried at ambient temperature to obtain G2 triazolyl chalcone dendrimer stabilized $Co@TiO_2$ core-shell nanoparticles. Similarly, the reaction is repeated to obtain PVP stabilized $Co@TiO_2$ core-shell nanoparticles

of molar ratio 1:1. The composite material thus obtained consists mostly of core-shell nanoparticles.

2.2. Characterization techniques.

The as-prepared nanoparticles were subjected to different characterization techniques. The prepared sample's crystal structure and phase analysis were studied using a powder X-ray diffractometer (D8 Advance Bruker) of Cu Kα radiation where λ = 1.5406 Å. The XRD pattern was obtained for the 2θ range from 10° to 80°. The optical studies of the synthesized nanoparticles were carried out using a UV–Vis spectrophotometer (Perkin Elmer LAMBDA 950) and Photoluminescence (PL) (JY-Horiba, Flurolog 3 spectra Fluorometer. The light source used in UV characterization was a Deuterium lamp with a wavelength of ± 0.08 nm and resolution of ≤ 0.05 nm. The source of PL was a xenon lamp recorded at room temperature, which provided optimum performance for highly scattering samples. The FTIR (Bruker-Alpha Platinum) was carried out on the sample, with Nernst Glower as the source, with a wavenumber ranging from 500 to 4000 cm^{-1}. XPS (ULVAC-PHI, Inc.; Model:PHI5000 Version Probe III) studied the elemental composition of the nanoparticles with the binding energy ranging from 0 to 1000 eV. The biological studies, namely, antifungal activity, were carried out by Apex Biotechnology Training and Research Institute.

3. Results and Discussion

3.1. Structural and morphological analyses.

3.1.1. XRD.

Figure 1(a) displays the XRD patterns for Co@TiO_2 core-shell nanoparticles synthesized using PVP as a stabilizing agent in Co@TiO_2 – A and second-generation (G2) triazolyl chalcone dendrimer as a stabilizing agent in Co@TiO_2 – B. The figure reflects the peaks that perfectly match the TiO_2 crystal system [26] in both samples. The narrow peaks with appropriate intensity ensure the crystallinity of the given samples. Some of the detected peaks match with the core element Cobalt (Co) of a hexagonal primitive crystal system belonging to the space group of $P6_3/mmc$ (JCPDS No. 897373). The diffraction peaks of Co at Co@TiO_2 – A at 2θ of 41°36', 41°36' and 41°36' can be indexed to (100), (002) and (102) respectively. Some of the diffraction peaks of Co have also been detected in Co@TiO_2 –B (Figure 1a). From this, we infer that Co nanoparticles were also present without the coating of TiO_2 in the sample.TiO_2, which is acting as shell material, is exhibited predominately as tetragonal primitive crystal system of space group $P4_2/mnm$ (JCPDS card no.841284) at 2θ of 27°57', 36°19', 39°30', 54°41', 56°71', 64°13', 69°28' and 69°88' indexed to (110), (101), (200), (211), (220), (310), (301) and (112) for the sample Co@TiO_2 – A. But in a few cases, it is also exhibited as a tetragonal body-centered crystal system at 2θ of 25°44', 37°90' and 48°14' indexed to (101), (004) and (200), respectively. As per the reports [27], the existence of diffraction peaks at both primitive and tetragonal body-centered cells can be detected only in the anatase phase of TiO_2. On the other hand, the rutile and brookite phase belongs to a simple tetragonal crystal system in which the tetragonal body-centered cell and the primitive cell are the same [28,29].

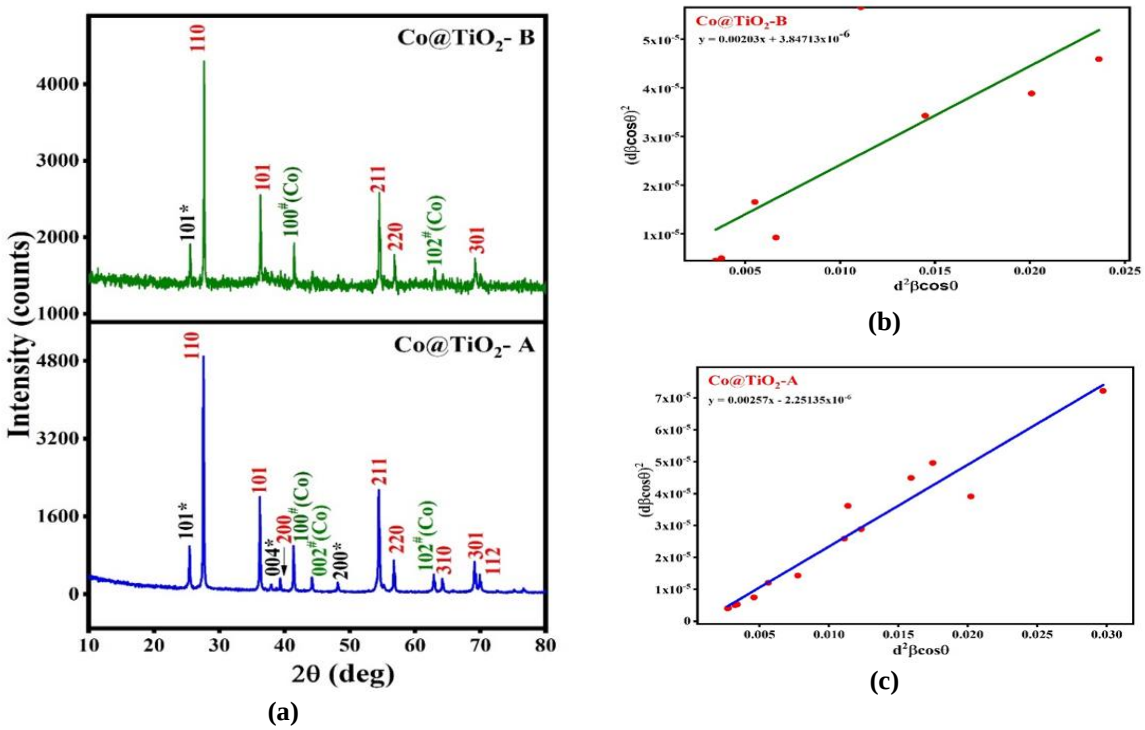

Figure 1. (a) XRD pattern of the synthesized samples; **(b)**Size – Strain Plot (SSP) for Co@TiO_2 - B; (c) Co@TiO_2 - A

In the present work, cobalt cores exhibit a hexagonal primitive crystal structure, and the TiO_2 shell possesses a tetragonal primitive crystal phase. This kind of mixed-phase present in the core-shell nanoparticles leads to non-spherical shell growth at particular crystallographic directions. Also, the analysis of intensity ratios among the two samples displays that sample B has more definite and qualitative peaks than the other [30]. The percentage of contraction in the inter-planar spacing 'd' is calculated by comparing the d-spacing value obtained from the XRD pattern with the JCPDS data card, and the results are given in Table 1.

Table 1. Comparison of Inter-planar spacing (dhkl) from XRD, JCPDS data card for corresponding (h k l) planes for Co@TiO_2 – A and Co@TiO_2 – B.

Stabilizing Agent	(h k l)	d_{XRD} (Å)	d_{JCPDS} (Å)	% of contraction in d	FWHM (deg)
PVP	110	3.2352	3.2432	0.2472	0.1141
	101	2.4816	2.4835	0.0766	0.1712
	211	1.6846	1.6848	0.0118	0.1044
	220	1.6215	1.6216	0.0062	0.1392
	301	1.3573	1.3578	0.0368	0.1044
G2	110	3.2247	3.2432	0.5737	0.1141
	101	2.4754	2.4835	0.3272	0.1427
	211	1.6837	1.6848	0.0653	0.0856
	220	1.6205	1.6216	0.0679	0.0856
	301	1.3568	1.3578	0.0737	0.2088

3.1.1.1. Scherrer method.

It is one of the simplest and prime methods to calculate the size and strain of the samples. Using the Scherrer equation (eq-1),

$$D = \frac{0.9\lambda}{\beta cos\theta} \quad (1)$$

Where, the wavelength (λ) of CuKα is taken as 1.5406Å, β is the full-width half maximum, and θ is the diffraction angle, the average crystallite size of the synthesized samples were calculated as 69 nm and 73 nm for Co@TiO_2 (A) and (B) respectively. Also, from the

calculated value of crystallite size, the dislocation density that gives the presence of crystal defects can be obtained using the formula;

$$\delta = \frac{1}{D^2}\ nm^{-1} \quad (2)$$

Similarly, the lattice strain (ε) for the synthesized samples can be obtained from the full width half maximum values and the diffraction angle using the formula,

$$\varepsilon = \frac{\beta cos\theta}{4sin\theta} \quad (3)$$

Thus, the calculated values were compared with graphical values obtained through a size-strain plot and displayed in Table 2.

3.1.1.2. Size-strain plot.

A size strain plot is one of the valid methods to evaluate the size strain parameter. In this method, the data reflected from lower angles were considered more prominent than the data reflected from higher angles as they are comparatively lower in preciseness than the former. In this approximation, the Lorentzian function describes the crystallite size, and the Gaussian function describes the strain.

$$(d\beta cos\theta)^2 = \frac{k}{D(d^2\beta cos\theta)+\left(\frac{\varepsilon}{2}\right)^2} \quad (4)$$

Here, k is '1' for non-spherical nanoparticles. In this size strain plot, the root of the y-intercept denotes the strain, and the slope of the linear fitted data gives the particle size of the sample.

Strain is measured in terms of the difference between the reference and observed d-spacing values [31]. Table- 1 shows the percentage of contraction between the two samples, which in turn reveals the strain induced on the sample. The results obtained throw light on the fact that G2 encapsulated Co@TiO_2 nanoparticles experience more strain than the other. Also, from the results obtained from SSP displayed in Table 2, it is clear that the strain on sample B (0.0019) is quite higher than in sample A.

Table 2. Structural parameters.

Sample	Intercept	Crystallite size (nm)	Strain	Crystallite size (nm)	Strain	Dislocation Density ($x10^{15}m^2$)
		Scherrer method		Size Strain Plot (SSP)		
PVP	$2.251x10^{-6}$	69	0.0014	59	0.0015	0.2043
G2	$3.847x10^{-6}$	73	0.0015	75	0.0019	0.1872

As per Gamler *et al*. [32] and others [33–35], the lattice mismatch between core shells induces strain and optimizes the performance of the sample as the shell thickness increases. Therefore, a thorough understanding of strain in individual core-shell nanoparticles is crucial as it affects the electronic structure of the particles and plays a significant role in catalysis applications. So here, G2 encapsulated Co@TiO_2 nanoparticles (sample B) are expected to show a better performance in their properties due to the induced strain by the capping agent (dendrimer) on the shell material.

3.1.2. FTIR.

Fourier Transform Infrared Spectrum has been recorded for the synthesized samples viz. Co@TiO_2 – A and Co@TiO_2 – B core-shell nanoparticles. From the spectrum, it is clear that the Co@TiO_2 – A shows minor peaks across 3280 cm^{-1}, 1639 cm^{-1}, 1343 cm^{-1}, 1001 $cm^{-1,}$ and 479 cm^{-1} whereas Co@TiO_2 – B has not recorded any sharp peaks but- it admits the presence of very weak signals across 2025 cm^{-1}, 1641 cm^{-1} and 470 cm^{-1} (Figure 2). As per the reports, the characteristic peaks at 470 cm^{-1} (Co@TiO_2 - A) and 479 cm^{-1} (Co@TiO_2 -B) can be assigned to the Ti-O stretching vibration. Fang Zhang *et al*., in their work on cobalt-based nanowires, have assigned Co-OH bonding to the peak occurring at 962 cm^{-1}. Similarly, the peak at 1001 cm^{-1} of Co@TiO_2 – A can be assigned to Co-OH bonding vibration [36]. The distinct band occurring at 1639 cm^{-1} and 1641 cm^{-1} has been assigned to carbonyl group vibrations, and the occurrence of a broad band at 3280 cm^{-1} is a result of the presence of absorbed water/moisture in the sample Co@TiO_2 –A [37]. Also, a weak peak of the sample Co@TiO_2 – B at 2025 cm^{-1} can be assigned to CH stretching vibrations of the dendrimer chain [38–40].

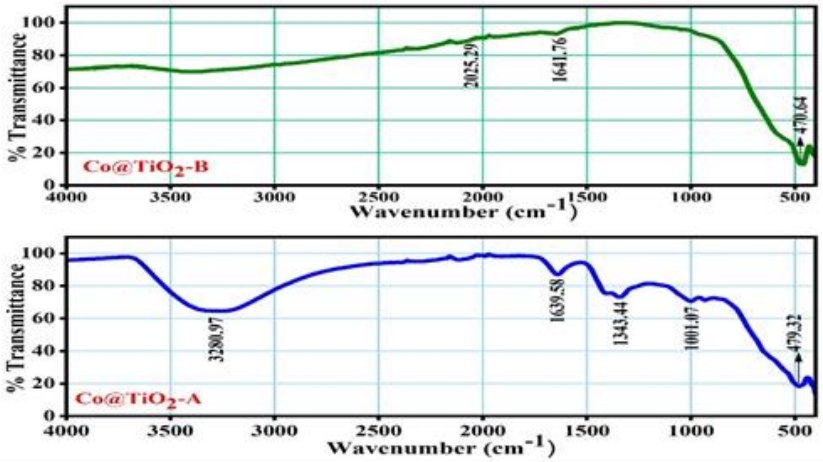

Figure 2. FTIR spectrum of Co@TiO_2 - A and Co@TiO_2 - B core-shell nanoparticles.

3.1.3. XPS.

The surface composition of the sample B (G2-Co@TiO_2) was analyzed using X-ray photoelectron spectroscopy (XPS). The chemical states of Ti in TiO_2 and Co in $Co(OH)_2$ are shown in Figure 3. Figure 3a shows the peaks of G2-chalcone dendrimer stabilized Co-TiO_2 nanoparticles that are observed in the survey spectrum. The surfaces of titanium oxide belong to the most established oxide systems in the science literature [41]. Titanium oxides are formed readily when Ti is exposed to an atmosphere containing water or oxygen due to their highly reactive nature towards oxygen. Also, the oxidation behavior of the metal is of interest for the properties of protective coatings [42–44]. In this study, the 2p spectrum of Titanium (Figure 3b) in TiO_2 is observed. The binding energy of Ti 2p appeared at 459.12 eV and 464.66 eV in the XPS spectrum, corresponding to Ti $2p_{3/2}$ and Ti $2p_{1/2,}$ respectively. The difference in their binding energy (ΔB.E) is calculated as 5.54 eV, which is consistent with the +4 oxidation state of Ti, and this confirms the formation of the pure anatase phase of TiO_2 [45,46].

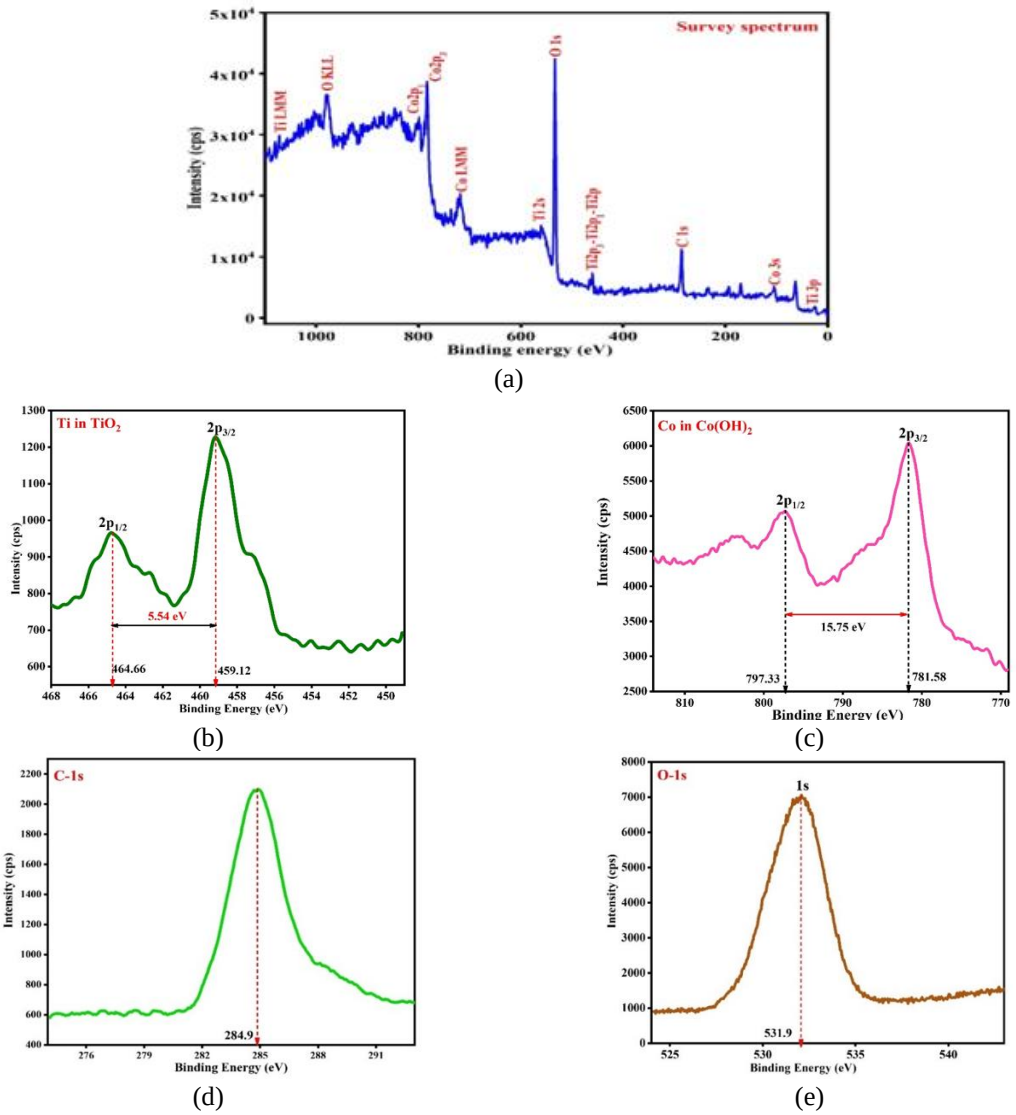

(a) (b) (c) (d) (e)

Figure 3. XPS spectrum of second generation chalcone dendrimer stabilized Co@TiO_2 core-shell nanoparticles. **(a)** survey spectrum; **(b)** Ti in TiO_2; **(c)** Co in $Co(OH)_2$; **(d)** C-1s; **(e)** O-1s.

The binding energy value of O1s is observed at 531.9 eV (Figure 3e) with a positive shift of 0.9 eV from its theoretical value (531 eV), which is attributed to the lattice oxygen of TiO_2. From Figure 3d, the presence of the C 1s spectrum can be seen near the binding energy of 284.8 eV. Fig 3c shows that two major peaks located at the binding energy 781.58 eV and 797.33 eV appeared to result from Co $2p_{3/2}$ and Co $2p_{1/2}$, respectively, with a splitting of 15.75 eV. The results are in good agreement with the reported value. The presence of Co2p in the $Co(OH)_2$ peak has a significant split of spin-orbit components. From the survey spectrum (Figure 3a), the Co2p region overlaps some of its weaker Co LMM Auger peaks and care must be taken to avoidis interpret the peak as an XPS peak [47,48].

3.2. Optical studies.

3.2.1. UV-absorption spectroscopy.

The optical properties of the samples Co@TiO_2 - A and Co@TiO_2 - B were analyzed using UV-Vis absorption spectroscopy and plotted as shown in Figure 4. In this technique, we record the incident photon wavelength from 200 to 800 nm as the electronic transition occurring due to the absorption of light by the electrons happens in the UV and visible regions

[49,50]. Figure 4 shows that the UV-Vis spectra show maximum absorption wavelength (λmax) for samples A and B at the same region, around 336 nm, irrespective of the stabilizing agents used. That is, the absorption peak, which is due to intrinsic band-band transition in the UV region, indicates that TiO_2 exhibits strong absorption in the UV region [51]. The additional broad peak at 698 nm in sample A corresponding to the red absorption in the visible region may be due to the electronic interaction between the core and shell (i.e.) broad absorption peak appearing in sample A may be due to the d-d electronic transitions of Co^{2+} in octahedral coordination, whereas, sample B shows high transparency in the visible region [52–54].

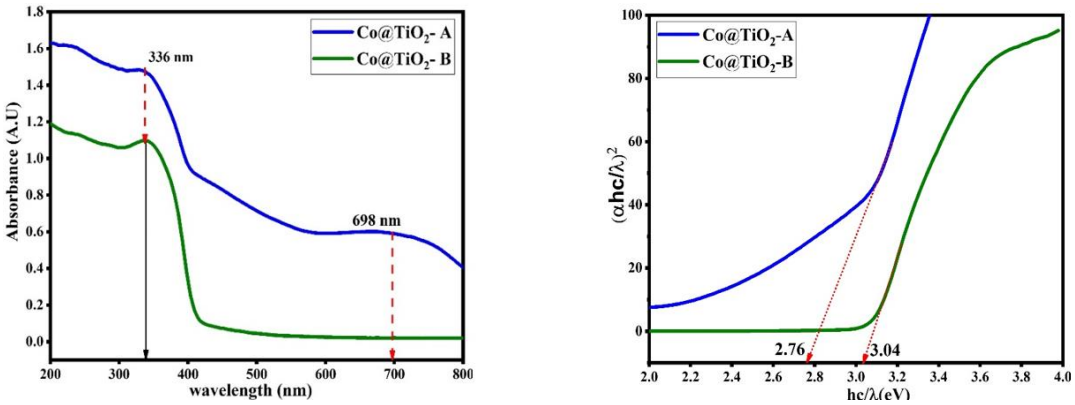

Figure 4. (a) UV absorption spectra; **(b)** Band gap energy spectra of Co@TiO2 -A and Co@TiO2 -B.

Figure 4b shows the band gap energy for the samples Co@TiO_2-A and Co@TiO_2-B as 2.76 eV and 3.04 eV, respectively. The band gap energy was evaluated using the Tauc plot method. This plot between $(\alpha hc/\lambda)^2$ and (hc/λ) identifies the type of electron transition occurring in Co@TiO_2 core-shell nanoparticles. Here, when the second generation triazolyl chalcone dendrimer [55] is used as the stabilizing agent (sample B) over PVP (sample A), the former exhibits broadening of the band gap (3.04 eV), which is 0.28 eV than the sample A. Interestingly, earlier reports of G2 used as a stabilizer in Ag@SnO_2 it also shows a similar pattern of band gap widening but not wider when compared to the bulk TiO_2 band gap 3.2 eV. Therefore, we conclude that when G2 triazolyl chalcone dendrimer is used as a stabilizer, it undergoes the Burstein – Moss (B-M) effect [54]. According to this effect, the dopant ions occupy the low energy levels, resulting in larger electron carrier concentration, which causes the fermi energy level to shift closer to the conduction band, making the band gap wider [56]. In this study, we infer that the Co@TiO_2 core-shell nanoparticles with G2 chalcone dendrimer as a stabilizing agent exhibit a wider band gap than the other.

3.2.2. Photoluminescence studies.

The photoluminescence spectrum of Co@TiO_2 - A and Co@TiO_2 - B is shown in Figure 5. From the figure, we can identify that though both the samples show almost similar patterns of the emission wavelength, the peaks are smoother in sample B, where the G2 dendrimer acts as the stabilizer. In sample B, due to the excitation wavelength of 325 nm, prominent emission peaks appear in the visible region at 420 nm and 467 nm.

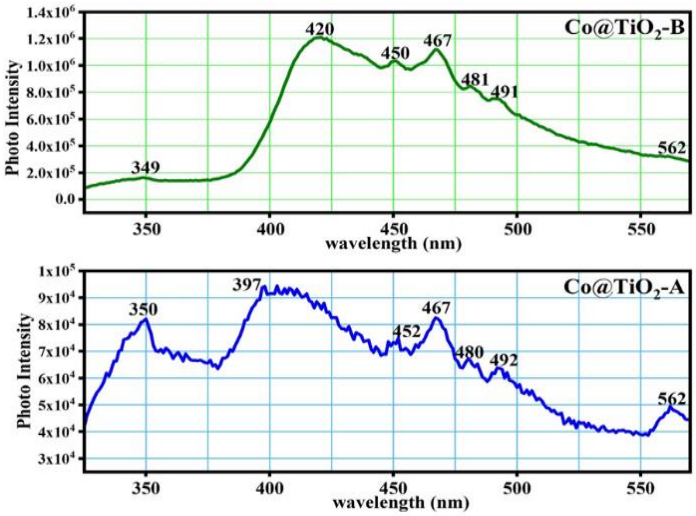

Figure 5. Photoluminescence spectrum of Co@TiO_2 - A and Co@TiO_2 – B.

The existence of stable excitons with the same energy is the cause for the similar peak positions appearing in samples A and B. As reported in the previous work [57], when zeroth generation triazolyl chalcone dendrimer (G_0) is used as the stabilizing agent for the core-shell nanoparticles Co@TiO_2, it exhibited two obvious PL peaks at 414 nm and 446 nm emitting photons at visible violet region. Here in this study, the sample with second-generation chalcone dendrimer (G_2) exhibits a wide PL signal at a range of 420 nm to 562 nm, covering weak peak signals at 420 nm, 450 nm, 467 nm, 481 nm, 491 nm, and 562 nm emitting photons at visible violet, blue and green regions. The visible luminescence is mainly attributed to structural defects and oxygen vacancies [58, 59].

The peaks that appear between 400 and 550 nm are mainly due to the surface oxygen vacancies. At the beginning, a small bump at 349 nm is seen, indicative of a band-edge ultraviolet (UV) emission originating from the TiO_2 host material. This is due to the phonon-assisted indirect transition from the edge (X) to the center (Γ) of the Brillouin zone. At high excitation, the electron-hole plasma state is the cause of violet emission at 420 nm [58,59]. A blue luminescence at 467 nm, 481 nm, and 491 nm is attributed to the surface oxygen vacancies, and in particular, the peak observed at 491 nm is due to the charge transfer band associated with oxygen vacancies [60,61]. Green luminescence is attributed to a weak peak signal observed at 562 nm.

Also, from Figure (5), we observe an increase in photo intensity for the sample Co@TiO_2 – B when compared to Co@TiO_2 –A. The increase in emission peak intensity with no appreciable peak shifting may be due to the destruction of a large number of non-radiative centers and a good crystalline nature when G2 acts as a stabilizing agent.

3.3. Biological studies.

3.3.1. Antifungal activity of Co@TiO_2 –B core-shell nanoparticles.

3.3.1.1. Pathogenic test of microorganisms.

The fungal mycelial pathogen *Aspergillus niger* (MTCC 404) and yeast pathogen *Candida albicans* (MTCC 227) are used for *in vitro* antifungal activity. The selected pathogens strains are obtained from the microbiological division.

3.3.1.2. *In vitro* antifungal activity.

The antifungal activity was determined by well diffusion methods [58,59], as shown in Figure 6. About 25 mL of potato dextrose agar was poured into a sterile petri plate (Himedia, Mumbai, India). The plates were allowed to solidify, and after three days there grew a 100 µl fungal spore suspension (10^5 cfu/mL) of mycelial fungal strain and 18 h old yeast strain adjusted with (10^5 cfu/mL) was swabbed using a sterile cotton swab on the agar plate, and the wells were made. The test samples were loaded into wells with various concentrations, such as 50 µg/well, 100 µg/well, 150 µg/well, 200 µg/well, and 30 µg/well of Clotrimazole added well served as the positive control. All the drug-loaded plates were kept for 24 -72 hours. The antifungal activity was determined by measuring the diameter of the zone of inhibition around the well using the antibiotic zone scale (Himedia, Mumbai, India).

Aspergillus niger Candida albicans

a: 0 µl/mL; b: 50 µg/mL; c: 100 µg/mL; d: 150 µg/mL; e: 200 µg/mL; f: Clotrimazole (30 µg/mL)

Figure 6. Antifungal activity of Co@TiO_2 –B core-shell nanoparticle.

3.3.1.3. Antifungal activity.

The given sample Co@TiO_2 –B is active against both pathogens. When the concentration of the test sample is increased, the sample shows high activity toward the tested pathogen. Table 3 shows the zone of inhibition against the test pathogen, and Clotrimazole at a concentration of 30µg was used as the standard drug of choice. In the present work, we note that the sample Co@TiO_2 –B shows double-fold activity against the test pathogen Candida albicans when compared to Aspergillus niger. The sample displays the highest activity at the zone of inhibition level of 30 mm against Candida albicans at the highest concentration. From Table 3, we can observe a trend of increased concentration, showing good antifungal activity.

Table 3. Antifungal activity of Co@TiO_2 –B core-shell nanoparticles.

Name of the sample	**ZOI (mm)**					**ZOI (mm) Standard***
	0 µg/mL	50 µg/mL	100 µg/mL	150 µg/mL	200 µg/mL	30 µg/well
Aspergillus niger	-	13	14	15	16	20
Candida albicans	-	23	25	28	30	20

As reported in our previous studies [62-65], when zeroth generation dendrimer (G_0) is used as the stabilizing agent in Co@TiO_2, the sample showed good activity against the test pathogen *Candida albicans*, i.e., the zone of inhibition for 100 µg/mL is 19mm. Also, the sample recorded mild activity against the test pathogen *Aspergillus niger*, i.e., the zone of inhibition for 100 µg/mL is 11 mm. Now in the present work, when the higher generation dendrimer (G_2) is used as the stabilizing agent in Co@TiO_2, the sample shows strong activity against *Candida albicans* (ZOI for 100 µg/mL is 25mm) and improved activity against

Aspergillus niger (ZOI for 100 µg/mL is 14 mm). (See Table 3). Also, as the concentration increases, the activity improves. In general, the sustained release of TiO_2 nanoparticles ensures the inactivity of cells. When the test pathogen is exposed to a higher sample dosage, the cells fail to withstand the direct interaction of nanoparticle exposure and cause cell death [66]. Therefore, it is clear that the viability of the cell completely depends on the concentration and exposure time of the sample, which plays a significant role in fungal activity [67,68].

4. Conclusions

In the current study, Co@TiO_2 core-shell nanoparticles were synthesized using second-generation (G2) chalcone dendrimer as stabilizing agent and treated against the most common fungal pathogens, *Candida albicans* and *Aspergillus niger*. The result shows that the sample exhibits stronger activity against the pathogens, and the acitivity improves concentration and increases it. Our previous study reported that while using G0 as a stabilizing agent, the synthesized sample showed moderate activity against the fungal pathogens. Therefore, we consolidate that higher-generation chalcone dendrimers, when used as stabilizing agents in Co@TiO_2, show stronger activity against the selected pathogens than the low-generation dendrimers.

Funding

This research received no external funding.

Acknowledgments

We thank Dr.S.Selvarani, Asst. Professor, Dept. of Chemistry, A.N.J. Ammal College, Sivakasi, India, for her support during the preparation of the sample.

Conflicts of Interest

The authors declare no conflict of interest.

References

1. Xu, X.; Dutta, A.; Khurgin, J.; Wei, A.; Shalaev, V.M.; Boltasseva, A. TiN@TiO $_2$ Core–Shell Nanoparticles as Plasmon-Enhanced Photosensitizers: The Role of Hot Electron Injection. *Laser Photonics Rev.* **2020**, *14*, 1900376, https://doi.org/10.1002/lpor.201900376.
2. Najafi, F.; Salami-Kalajahi, M.; Roghani-Mamaqani, H. A review on synthesis and applications of dendrimers. *J. Iran. Chem. Soc.* **2021**, *18*, 503–517, https://doi.org/10.1007/s13738-020-02053-3.
3. Tripathi, P.K.; Gupta, S.; Rai, S.; Shrivatava, A.; Tripathi, S.; Singh, S.; Khopade, A.J.; Kesharwani, P. Curcumin loaded poly (amidoamine) dendrimer-plamitic acid core-shell nanoparticles as anti-stress therapeutics. *Drug Dev. Ind. Pharm.* **2020**, *46*, 412–426, https://doi.org/10.1080/03639045.2020.1724132.
4. Ghiasi, A.; Malekpour, A. Octyl coated cobalt-ferrite/silica core-shell nanoparticles for ultrasonic assisted-magnetic solid-phase extraction and speciation of trace amount of chromium in water samples. *Microchem. J.* **2020**, *154*, 104530, https://doi.org/10.1016/j.microc.2019.104530.
5. Fateh, S.T.; Aghaii, A.H.; Aminzade, Z.; Shahriari, E.; Roohpour, N.; Koosha, F.; Dezfuli, A.S. Inorganic nanoparticle-cored dendrimers for biomedical applications: A review. *Heliyon* **2024**, *10*, e29726, https://doi.org/10.1016/j.heliyon.2024.e29726.
6. Murugesan, K.; Chandrashekhar, V.G.; Kreyenschulte, C.; Beller, M.; Jagadeesh, R.V. A General Catalyst Based on Cobalt Core–Shell Nanoparticles for the Hydrogenation of N-Heteroarenes Including Pyridines. *Angew. Chem. Int. Ed.* **2020**, *59*, 17408, https://doi.org/10.1002/anie.202004674.

7. Ali, M.; Hussain, R.; Tariq, F.; Noreen, Z.; Toufiq, A.M.; Bokhari, H.; Akhtar, N.; Rahman, S.u. Highly effective visible light-activated cobalt-doped TiO_2 nanoparticles for antibacterial coatings against *Campylobacter jejuni*. *Appl. Nanosci.* **2020**, *10*, 1005-1012, https://doi.org/10.1007/s13204-019-01193-0.
8. Mayakannan, M.; Gopinath, S.; Vetrivel, S. Synthesis and characterization of antibacterial activities nickel doped cobalt oxide nano particles. *Mater. Chem. Phys.* **2020**, *242*, 122282, https://doi.org/10.1016/j.matchemphys.2019.122282.
9. Shi, D.; Yang, H.; Xue, X. Preparation, characterization and antibacterial properties of cobalt doped titania nanomaterials. *Chin. J. Chem. Eng.* **2020**, *28*, 1474-1482, https://doi.org/10.1016/j.cjche.2020.03.017.
10. Watanabe, K.; Fukuzaki, S.; Sugino, A.; Benson, N.; Metcalf, N.; Nakamura, M.; Matsumoto, M. Cobalt–Chromium Alloy Has Superior Antibacterial Effect Than Titanium Alloy: In Vitro and In Vivo Studies. *Spine* **2021**, *46*, E911–E915, https://doi.org/10.1097/BRS.0000000000003970.
11. Tao, B.; Lin, C.; He, Y.; Yuan, Z.; Chen, M.; Xu, K.; Li, K.; Guo, A.; Cai, K.; Chen, L. Osteoimmunomodulation mediating improved osteointegration by OGP-loaded cobalt-metal organic framework on titanium implants with antibacterial property. *Chem. Eng. J.* **2021**, *423*, 130176, https://doi.org/10.1016/j.cej.2021.130176.
12. Karthikeyan, K.; Chandraprabha, M.N.; Hari Krishna, R.; Samrat, K.; Sakunthala, A.; Sasikumar, M. Optical and antibacterial activity of biogenic core-shell ZnO@TiO_2 nanoparticles. *J. Indian Chem. Soc.* **2022**, *99*, 100361, https://doi.org/10.1016/j.jics.2022.100361.
13. L, K.B.; Y.V, R.R. "Synthesis and Characterization of Magnetically Core-Shell Structured $CoFe_2O_4$/SiO_2 Nanoparticles; Their Enhanced Antibacterial and Electrocatalytic Properties". *Colloids Surf. A: Physicochem. Eng. Asp.* **2020**, *598*, 124806, https://doi.org/10.1016/j.colsurfa.2020.124806.
14. Shanmuganathan, R.; LewisOscar, F.; Shanmugam, S.; Thajuddin, N.; Alharbi, S.A.; Alharbi, N.S.; Brindhadevi, K.; Pugazhendhi, A. Core/shell nanoparticles: Synthesis, investigation of antimicrobial potential and photocatalytic degradation of Rhodamine B. *J. Photochem. Photobiol. B: Biol.* **2020**, *202*,111729, https://doi.org/10.1016/j.jphotobiol.2019.111729.
15. Akhtar, S.; Shahzad, K.; Mushtaq, S.; Ali, I.; Rafe, M.H.; Fazal-ul-Karim, S.M. Antibacterial and antiviral potential of colloidal Titanium dioxide (TiO_2) nanoparticles suitable for biological applications. *Mater. Res. Express* **2019**, *6*, 105409, https://doi.org/10.1088/2053-1591/ab3b27.
16. YazdanYar, A.; Aschauer, U.; Bowen, P. Interaction of biologically relevant ions and organic molecules with titanium oxide (rutile) surfaces: A review on molecular dynamics studies. *Colloids Surf. B Biointerfaces* **2018**, *161*, 563-577, https://doi.org/10.1016/j.colsurfb.2017.11.004.
17. Berman, J.; Hadany, L. Does stress induce (para)sex? Implications for *Candida albicans* evolution. *Trends Genetics* **2012**, *28*, 197-203, https://doi.org/10.1016/j.tig.2012.01.004.
18. Sudbery, P.; Gow, N.; Berman, J. The distinct morphogenic states of *Candida albicans*. *Trends Microbiol.* **2004**, *12*, 317-324, https://doi.org/10.1016/j.tim.2004.05.008.
19. Schuster, E.; Dunn-Coleman, N.; Frisvad, J.; van Dijck, P. On the safety of *Aspergillus niger* – a review. *Appl. Microbiol. Biotechnol.* **2002**, *59*, 426-435, https://doi.org/10.1007/s00253-002-1032-6.
20. Baker, S.E. *Aspergillus niger* genomics: Past, present and into the future. *Med. Mycol.* **2006**, *44*, S17-S21, https://doi.org/10.1080/13693780600921037.
21. Kathiravan, M.K.; Salake, A.B.; Chothe, A.S.; Dudhe, P.B.; Watode, R.P.; Mukta, M.S.; Gadhwe, S. The biology and chemistry of antifungal agents: A review. *Bioorg. Med. Chem.* **2012**, *20*, 5678-5698, https://doi.org/10.1016/j.bmc.2012.04.045.
22. Algahtani, F.D.; Elabbasy, M.T.; Asghar, A.H.; Elhassan, N.E.; Gdaim, S.; El-Morsy, M.A.; Farea, M.O.; Menazea, A.A. Tunning Silver@Gold core@shell incorporated in poly (vinyl alcohol) via laser ablation: Antibacterial activity and cell viability behavior for wound healing. *J. Saudi Chem. Soc.* **2023**, *27*, 101637, https://doi.org/10.1016/j.jscs.2023.101637.
23. Huang, P.; Zhang, Y.; Wang, B.; Zhu, X.; He, Y.; Song, P.; Wang, Z.; Wang, R. Synthesis of acryloyl copolymer core–shell microspheres with antibacterial activity and surface cationic effects. *J. Mater. Sci.* **2023**, *58*, 7718-7730, https://doi.org/10.1007/s10853-023-08475-7.
24. Mubarak, M.F.; Selim, H.; Elshypany, R. Hybrid magnetic core–shell TiO_2@$CoFe_3O_4$ composite towards visible light-driven photodegradation of Methylene blue dye and the heavy metal adsorption: isotherm and kinetic study. *J. Environ. Health Sci. Eng.* **2022**, *20*, 265-280, https://doi.org/10.1007/s40201-021-00774-y.
25. Sharda, D.; Choudhury, D. Insulin–cobalt core–shell nanoparticles for receptor-targeted bioimaging and diabetic wound healing. *RSC Adv.* **2023**, *13*, 20321-20335, https://doi.org/10.1039/D3RA01473H.

26. Baldini, E.; Chiodo, L.; Dominguez, A.; Palummo, M.; Moser, S.; Yazdi-Rizi, M.; Auböck, G.; Mallett, B.P.P.; Berger, H.; Magrez, A.; Bernhard, C.; Grioni, M.; Rubio, A.; Chergui, M. Strongly bound excitons in anatase TiO_2 single crystals and nanoparticles. *Nat. Commun.* **2017**, *8*, 13, https://doi.org/10.1038/s41467-017-00016-6.
27. Jolivet, A.; Labbé, C.; Frilay, C.; Debieu, O.; Marie, P.; Horcholle, B.; Lemarié, F.; Portier, X.; Grygiel, C.; Duprey, S.; Jadwisienczak, W.; Ingram, D.; Upadhyay, M.; David, A.; Fouchet, A.; Lüders, U.; Cardin, J. Structural, optical, and electrical properties of TiO_2 thin films deposited by ALD: Impact of the substrate, the deposited thickness and the deposition temperature. *Appl. Surf. Sci.* **2023**, *608*, 155214, https://doi.org/10.1016/j.apsusc.2022.155214.
28. Javed, R.; Zia, M.; Naz, S.; Aisida, S.O.; Ain, N.u.; Ao, Q. Role of capping agents in the application of nanoparticles in biomedicine and environmental remediation: recent trends and future prospects. *J. Nanobiotechnol.* **2020**, *18*, 172, https://doi.org/10.1186/s12951-020-00704-4.
29. Ludescher, L.; Dirin, D.N.; Kovalenko, M.V.; Sztucki, M.; Boesecke, P.; Lechner, R.T. Impact of Crystal Structure and Particles Shape on the Photoluminescence Intensity of CdSe/CdS Core/Shell Nanocrystals. *Front. Chem.* **2019**, *6*, 672, https://doi.org/10.3389/fchem.2018.00672.
30. Gamler, J.T.L.; Leonardi, A.; Sang, X.; Koczkur, K.M.; Unocic, R.R.; Engel, M.; Skrabalak, S.E. Effect of lattice mismatch and shell thickness on strain in core@shell nanocrystals. *Nanoscale Adv.* **2020**, *2*, 1105-1114, https://doi.org/10.1039/D0NA00061B.
31. Himabindu, B.; Latha Devi, N.S.M.P.; Rajini Kanth, B. Microstructural parameters from X-ray peak profile analysis by Williamson-Hall models; A review. *Mater. Today Proc.* **2021**, *47*, 4891-4896, https://doi.org/10.1016/j.matpr.2021.06.256.
32. Suresh, A.; Soundararajan, N. The conventional cell and the primitive cell electronic structure of anatase titanium dioxide crystal. *Mater. Res. Express* **2017**, *4*, 036301, https://doi.org/10.1088/2053-1591/aa5e5e.
33. Chung, J.; Rabenberg, L. Effects of strain gradients on strain measurements using geometrical phase analysis in the transmission electron microscope. *Ultramicroscopy* **2008**, *108*, 1595-1602, https://doi.org/10.1016/j.ultramic.2008.05.010.
34. Leonardi, A.; Leoni, M.; Li, M.; Scardi, P. Strain in Atomistic Models of Nanocrystalline Clusters. *J. Nanosci. Nanotechnol.* **2012**, *12*, 8546-8553, https://doi.org/10.1166/jnn.2012.6807.
35. Solla-Gullon, J.; Garnier, E.; Feliu, J.M.; Leoni, M.; Leonardi, A.; Scardi, P. Structure and morphology of shape-controlled Pd nanocrystals. *J. Appl. Crystallogr.* **2015**, *48*, 1534-1542, https://doi.org/10.1107/S1600576715015964.
36. Zhang, F.; Yuan, C.; Lu, X.; Zhang, L.; Che, Q.; Zhang, X. Facile growth of mesoporous Co_3O_4 nanowire arrays on Ni foam for high performance electrochemical capacitors. *J. Power Sources* **2012**, *203*, 250-256, https://doi.org/10.1016/j.jpowsour.2011.12.001.
37. D'Amelia, R.P.; Mancuso, J.; Nirode, W. The Characterization of Poly n-Vinyl Pyrrolidone-Polyvinyl Acetate (PVP-PVAc) Copolymers and Blends by Nuclear Magnetic Resonance Spectroscopy, Fourier Transform Infrared Spectroscopy, and Elemental Analysis. *J. Polym. Biopolym. Phys. Chem.* **2019**, *7*, 1-9, https://doi.org/10.12691/jpbpc-7-1-1.
38. Ling, M.F.C.; Hui, K.C.; Sambudi, N.S. Modification of TiO_2 with clam-shell powder for photodegradation of methylene blue. *J. Sol-Gel Sci. Technol.* **2022**, *102*, 412-421, https://doi.org/10.1007/s10971-022-05761-9.
39. Li, Y.; Luo, R.; Zhao, Q.; Guo, T.; Wu, J.; Peng, Z.; Wang, B.; Xu, R.; Ye, C. Preparation and characterization of cobalt–titanium dioxide on the surfaces of titanium implants. *Mater. Express* **2022**, *12*, 878-885, https://doi.org/10.1166/mex.2022.2234.
40. Barani, M.; Rahdar, A.; Mukhtar, M.; Razzaq, S.; Qindeel, M.; Hosseini Olam, S.A.; Paiva-Santos, A.C.; Ajalli, N.; Sargazi, S.; Balakrishnan, D.; Gupta, A.K.; Pandey, S. Recent application of cobalt ferrite nanoparticles as a theranostic agent. *Mater. Today Chem.* **2022**, *26*, 101131, https://doi.org/10.1016/j.mtchem.2022.101131.
41. Tunc, I.; Bruns, M.; Gliemann, H.; Grunze, M.; Koelsch, P. Bandgap determination and charge separation in $Ag@TiO_2$ core shell nanoparticle films. *Surf. Interface Anal.* **2010**, *42*, 835-841, https://doi.org/10.1002/sia.3558.
42. Fu, N.; Ren, X.-c.; Wan, J.-x. Preparation of Ag-Coated $SiO_2@TiO_2$ Core-Shell Nanocomposites and Their Photocatalytic Applications towards Phenol and Methylene Blue Degradation. *J. Nanomater.* **2019**, *2019*, 8175803, https://doi.org/10.1155/2019/8175803.

43. Wang, J.; Chen, W.; Hu, X.; Chen, B.; Zhang, Z.; Jiang, L.; Jiang, X. Effect of Fe doped Co–Ni protective coatings on the oxidation behavior and electrical properties of SOFC alloy interconnect materials. *Ceram. Int.* **2024**, *50*, 22960-22973, https://doi.org/10.1016/j.ceramint.2024.04.020.
44. Lee, J.-W.; Kong, S.; Kim, W.-S.; Kim, J. Preparation and characterization of SiO_2/TiO_2 core-shell particles with controlled shell thickness. *Mater. Chem. Phys.* **2007**, *106*, 39-44, https://doi.org/10.1016/j.matchemphys.2007.05.019.
45. Du, J.; Zhang, J.; Liu, Z.; Han, B.; Jiang, T.; Huang, Y. Controlled Synthesis of Ag/TiO_2 Core−Shell Nanowires with Smooth and Bristled Surfaces via a One-Step Solution Route. *Langmuir* **2006**, *22*, 1307-1312, https://doi.org/10.1021/la052337q.
46. Sahay, A.; Tomar, R.S.; Shrivastava, V.; Chauhan, P.S. Eugenol Loaded Ag-Ti-Co Nanocomposite as a Promising Antimicrobial and Antioxidative Agent. *BioNanoScience* **2023**, *13*, 339-351, https://doi.org/10.1007/s12668-023-01093-2.
47. Kim, C.; Choi, M.; Jang, J. Nitrogen-doped SiO_2/TiO_2 core/shell nanoparticles as highly efficient visible light photocatalyst. *Catal. Commun.* **2010**, *11*, 378-382, https://doi.org/10.1016/j.catcom.2009.11.005.
48. Wang, L.; Cheng, B.; Zhang, L.; Yu, J. In situ Irradiated XPS Investigation on S-Scheme $TiO_2@ZnIn_2S_4$ Photocatalyst for Efficient Photocatalytic CO_2 Reduction. *Small* **2021**, *17*, 2103447, https://doi.org/10.1002/smll.202103447.
49. Murali, N.; Mukherjee, D.; Das, S.B.; Dhillon, A.K.; Siddhanta, S.; Mallick, D.; Betal, S. Magnetoelectric Core–Shell Nanoparticle–Based Wearable Hybrid Energy Harvesters for Biomedical Applications. *Adv. Eng. Mater.* **2023**, *25*, 2301061, https://doi.org/10.1002/adem.202301061.
50. Hossain, S.; Hossain, S. Optical Characterization of Cobalt Ferrite and Magnetoelectric Cobalt Ferrite-Barium Titanate Core Shell Nanoparticles in Infra-Red Range. *IEEE Trans. Nanotechnol.* **2022**, *21*, 172-176, https://doi.org/10.1109/TNANO.2022.3160349.
51. Qiu, C.; Odarchenko, Y.; Lezcano-Gonzalez, I.; Meng, Q.; Slater, T.; Xu, S.; Beale, A.M. Visualising Co nanoparticle aggregation and encapsulation in Co/TiO_2 catalysts and its mitigation through surfactant residues. *J. Catal.* **2023**, *419*, 58-67, https://doi.org/10.1016/j.jcat.2023.02.002.
52. Chen, S.W.; Lee, J.M.; Lu, K.T.; Pao, C.W.; Lee, J.F.; Chan, T.S.; Chen, J.M. Band-gap narrowing of TiO_2 doped with Ce probed with x-ray absorption spectroscopy. *Appl. Phys. Lett.* **2010**, *97*, 012104, https://doi.org/10.1063/1.3460916.
53. Serpone, N.; Lawless, D.; Khairutdinov, R. Size Effects on the Photophysical Properties of Colloidal Anatase TiO2 Particles: Size Quantization versus Direct Transitions in This Indirect Semiconductor?. *J. Phys. Chem.* **1995**, *99*, 16646-16654, https://doi.org/10.1021/j100045a026.
54. Xu, C.X.; Sun, X.W.; Dong, Z.L.; Tan, S.T.; Cui, Y.P.; Wang, B.P. Manganese-doped zinc oxide tetratubes and their photoluminescent properties. *J. Appl. Phys.* **2005**, *98*, 113513, https://doi.org/10.1063/1.2138804.
55. Vanathi Vijayalakshmi, R.; Ravichandran, K.; Selvarani, S. Investigation on luminescence properties using second-generation (G2) triazolyl chalcone dendrimer as stabilizing agent in $Ag@SnO_2$ core–shell nanoparticles. *J. Mater. Sci.: Mater. Electron.* **2020**, *31*, 14295-14305, https://doi.org/10.1007/s10854-020-03986-4.
56. Yu, J.C.; Yu; Ho; Jiang; Zhang. Effects of F- Doping on the Photocatalytic Activity and Microstructures of Nanocrystalline TiO_2 Powders. *Chem. Mater.* **2002**, *14*, 3808-3816, https://doi.org/10.1021/cm020027c.
57. Vijayalakshmi, R.V.; Kuppan, R.; Kumar, P.P. Investigation on the impact of different stabilizing agents on structural, optical properties of $Ag@SnO_2$ core - shell nanoparticles and its biological applications. *J. Mol. Liq.* **2020**, *307*, 112951, https://doi.org/10.1016/j.molliq.2020.112951.
58. Wu, W.-Y.; Chang, Y.-M.; Ting, J.-M. Room-Temperature Synthesis of Single-Crystalline Anatase TiO_2 Nanowires. *Cryst. Growth Des.* **2010**, *10*, 1646-1651, https://doi.org/10.1021/cg901210c.
59. Serpone, N. Is the Band Gap of Pristine TiO_2 Narrowed by Anion- and Cation-Doping of Titanium Dioxide in Second-Generation Photocatalysts?. *J. Phys. Chem. B* **2006**, *110*, 24287-24293, https://doi.org/10.1021/jp065659r.
60. Zhang, C.; Feng, X.; Song, Q.; Zhou, C.; Peng, L.; Chen, J.; Liu, X.; Chen, H.; Lin, J.; Chen, X. Blue-Violet Emission with Near-Unity Photoluminescence Quantum Yield from Cu(I)-Doped Rb_3InCl_6 Single Crystals. *J. Phys. Chem. Lett.* **2021**, *12*, 7928-7934, https://doi.org/10.1021/acs.jpclett.1c01751.
61. Choudhury, B.; Choudhury, A. Luminescence characteristics of cobalt doped TiO_2 nanoparticles. *J. Lumin.* **2012**, *132*, 178-184, https://doi.org/10.1016/j.jlumin.2011.08.020.

62. Magaldi, S.; Mata-Essayag, S.; Hartung de Capriles, C.; Perez, C.; Colella, M.T.; Olaizola, C.; Ontiveros, Y. Well diffusion for antifungal susceptibility testing. *Int. J. Infect. Dis.* **2004**, *8*, 39-45, https://doi.org/10.1016/j.ijid.2003.03.002.
63. Shahriarinour, M.; Divsar, F.; Mehdipour, A.; Youseftabar-Miri, L.; Barkhordri, V. Antibacterial Properties of Cobalt Ferrite Magnetic Nanoparticles Loaded on Date Palm Pollen Against Multidrug-Resistant Bacteria. *Arab. J. Sci. Eng.* **2023**, *48*, 7315-7322, https://doi.org/10.1007/s13369-023-07811-y.
64. Rani, P.; Varma, R.S.; Singh, K.; Acevedo, R.; Singh, J. Catalytic and antimicrobial potential of green synthesized Au and Au@Ag core-shell nanoparticles. *Chemosphere* **2023**, *317*, 137841, https://doi.org/10.1016/j.chemosphere.2023.137841.
65. Vijayalakshmi, R.V.; Kumar, P.P.; Selvarani, S.; Rajakumar, P.; Ravichandran, K. Chalcone dendrimer stabilized core–shell nanoparticles—a comparative study on Co@ TiO_2, Ag@ TiO_2 and Co@ AgCl nanoparticles for antibacterial and antifungal activity. *Mater. Res. Express* **2017**, *4*, 105046, https://dx.doi.org/10.1088/2053-1591/aa90ef.
66. Hasan, S.; Khashan, K.S.; Hadi, A.A. Laser-Induced Synthesis of Palladium @ Silver Core–Shell NPs as an Effective Antibacterial Agent. *Plasmonics* **2023**, *18*, 689-699, https://doi.org/10.1007/s11468-023-01797-x.
67. Khalid, K.; Zahra, A.; Amara, U.; Khalid, M.; Hanif, M.; Aziz, M.; Mahmood, K.; Ajmal, M.; Asif, M.; Saeed, K.; Qayyum, M.F.; Abbas, W. Titanium doped cobalt ferrite fabricated graphene oxide nanocomposite for efficient photocatalytic and antibacterial activities. *Chemosphere* **2023**, *338*, 139531, https://doi.org/10.1016/j.chemosphere.2023.139531.
68. Namasivayam, S.K.R.; Vigneshwaraprakash, L.; Samrat, K.; Kavisri, M.; Meivelu, M.; Bharani, R.S.A. Enhanced Antibacterial Activity of Highly Biocompatible Polymeric Core–Shell Levofloxacin Gold Nanocomposite Formulation Against *Pseudomonas aeruginosa*. *Appl. Biochem. Biotechnol.* **2023**, *195*, 1837-1861, https://doi.org/10.1007/s12010-022-04256-1.